OPEN ACCESS

KING'S College LONDON

King's Research Portal

DOI:
10.1002/mrm.28577

Document Version
Publisher's PDF, also known as Version of record

Link to publication record in King's Research Portal

Citation for published version (APA):
López, K., Neji, R., Bustin, A., Rashid, I., Hajhosseiny, R., Malik, S. J., Teixeira, R. P. A. G., Razavi, R., Prieto, C., Roujol, S., & Botnar, R. M. (2021). Quantitative magnetization transfer imaging for non-contrast enhanced detection of myocardial fibrosis. *Magnetic Resonance in Medicine*, *85*(4), 2069-2083. https://doi.org/10.1002/mrm.28577

Citing this paper
Please note that where the full-text provided on King's Research Portal is the Author Accepted Manuscript or Post-Print version this may differ from the final Published version. If citing, it is advised that you check and use the publisher's definitive version for pagination, volume/issue, and date of publication details. And where the final published version is provided on the Research Portal, if citing you are again advised to check the publisher's website for any subsequent corrections.

General rights
Copyright and moral rights for the publications made accessible in the Research Portal are retained by the authors and/or other copyright owners and it is a condition of accessing publications that users recognize and abide by the legal requirements associated with these rights.

•Users may download and print one copy of any publication from the Research Portal for the purpose of private study or research.
•You may not further distribute the material or use it for any profit-making activity or commercial gain
•You may freely distribute the URL identifying the publication in the Research Portal

Take down policy
If you believe that this document breaches copyright please contact librarypure@kcl.ac.uk providing details, and we will remove access to the work immediately and investigate your claim.

Download date: 26. Oct. 2023

Received: 6 February 2020 | Revised: 10 September 2020 | Accepted: 9 October 2020

DOI: 10.1002/mrm.28577

FULL PAPER

Magnetic Resonance in Medicine

Quantitative magnetization transfer imaging for non-contrast enhanced detection of myocardial fibrosis

Karina López[1] | **Radhouene Neji**[1,2] | **Aurelien Bustin**[1] | **Imran Rashid**[1] | **Reza Hajhosseiny**[1] | **Shaihan J. Malik**[1] | **Rui Pedro A. G. Teixeira**[1] | **Reza Razavi**[1] | **Claudia Prieto**[1] | **Sébastien Roujol**[1] | **René M. Botnar**[1]

[1]School of Biomedical Engineering and Imaging Sciences, King's College London, London, UK

[2]MR Research Collaboration, Siemens Healthcare Limited, Frimley, UK

Correspondence
Karina Lopez, School of Biomedical Engineering and Imaging Sciences, King's College London, 3rd Floor Lambeth Wing, St Thomas' Hospital, Westminster Bridge Road, London SE1 7EH, UK.
Email karina.lopez@kcl.ac.uk

Funding information
National Institute for Health Research; Engineering and Physical Sciences Research Council, Grant/Award Number: EP/L015226/1, EP/P001009/1 and EP/P007619; Siemens Healthineers, Grant/Award Number: KL was co-funded by Siemens Healthcare GmbH; Wellcome EPSRC Centre For Medical Imaging, Grant/Award Number: NS/A000049/1 and WT 203148/Z/16/Z

Purpose: To develop a novel gadolinium-free model-based quantitative magnetization transfer (qMT) technique to assess macromolecular changes associated with myocardial fibrosis.

Methods: The proposed sequence consists of a two-dimensional breath-held dual shot interleaved acquisition of five MT-weighted (MTw) spoiled gradient echo images, with variable MT flip angles (FAs) and off-resonance frequencies. A two-pool exchange model and dictionary matching were used to quantify the pool size ratio (PSR) and bound pool T2 relaxation (T_2^B). The signal model was developed and validated using 25 MTw images on a bovine serum albumin (BSA) phantom and in vivo human thigh muscle. A protocol with five MTw images was optimized for single breath-hold cardiac qMT imaging. The proposed sequence was tested in 10 healthy subjects and 5 patients with myocardial fibrosis and compared to late gadolinium enhancement (LGE).

Results: PSR values in the BSA phantom were within the confidence interval of previously reported values (concentration 10% BSA = 5.9 ± 0.1%, 15% BSA = 9.4 ± 0.2%). PSR and T_2^B in thigh muscle were also in agreement with literature (PSR = 10.9 ± 0.3%, T_2^B = 6.4 ± 0.4 us). In 10 healthy subjects, global left ventricular PSR was 4.30 ± 0.65%. In patients, PSR was reduced in areas associated with LGE (remote: 4.68 ± 0.70% vs. fibrotic: 3.12 ± 0.78 %, $n = 5$, $P < .002$).

Conclusion: In vivo model-based qMT mapping of the heart was performed for the first time, with promising results for non-contrast enhanced assessment of myocardial fibrosis.

KEYWORDS
cardiac, fibrosis, gadolinium-free, magnetization transfer, quantitative mapping

This is an open access article under the terms of the Creative Commons Attribution License, which permits use, distribution and reproduction in any medium, provided the original work is properly cited.
© 2020 The Authors. *Magnetic Resonance in Medicine* published by Wiley Periodicals LLC on behalf of International Society for Magnetic Resonance in Medicine

1 | INTRODUCTION

The presence of scar following myocardial infarction has been shown to have important prognostic implications for patients with ischemic cardiomyopathy. Late gadolinium enhancement (LGE) MRI is the gold standard[1] for the assessment of myocardial replacement fibrosis, targeting the enlarged extracellular space with gadolinium-based contrast agents, so that an enhanced signal allows the localization of fibrotic tissue.[2] LGE is a highly effective approach for focal scar visualization and quantification; however, LGE does not allow diffuse fibrosis quantification as it visualizes contrast differences between normal and diseased myocardium. More recently, there has been an interest in quantification of local and diffuse fibrosis using T1 mapping with[3] or without[4] gadolinium-based contrast agents (GBCAs); yet, there remain questions about its sensitivity and specificity.[5] Also, the use of GBCAs may be associated with an increased risk of nephrogenic systemic fibrosis in patients with pre-existing renal dysfunction,[6] and there have been recent reports of long-term retention of some GBCAs in the brain.[7] Therefore, the development of quantitative and gadolinium-free approaches for assessment of myocardial fibrosis may be highly beneficial.

Magnetization transfer (MT) is an endogenous MR contrast that can be exploited to identify tissue with high macromolecular content. MT has been previously considered as a gadolinium-free alternative to LGE,[5] showing to be sensitive to an increase in collagen[8] and thus, with a potential for the assessment of myocardial scar.[9] In part due to its increased spin density and slow molecular motion, dephasing of the transverse magnetization is very efficient within large macromolecules, which typically translates into extremely short T2 relaxation times, on the order of a few microseconds, thus, making them impossible to detect by standard MRI techniques. However, in a seminal study, Wolff and Balaban[10] observed a signal loss in the water peak of up to a 30% in the kidney after off-resonance radiofrequency (RF) irradiation. Such preparation selectively saturates the extremely short T2 species of macromolecules while sparing the free-water spins, because of the broader resonance spectrum of macromolecules. Thus, the observed signal loss is due to the magnetization *transfer* (or exchange) that occurs between water spins bound to macromolecules and those that can move more freely.

One approach to quantify the MT effect is to obtain a ratio of the MT contrast change, by acquiring one image with MT contrast and one without it. Previous studies have explored the use of MT ratio (MTR) for gadolinium-free assessment of chronic or acute myocardial fibrosis. In vivo studies have shown reductions of the MT effects associated with both acute[11,12] and over 10-mo old myocardial infarction (MI).[13] A post-mortem study[9] found correlation between increased MTR and fibrous tissue in histology, while some areas of decreased MTR were associated with inflammatory granulocyte infiltration at a microscopic level. This shows that MTR results can be complex to interpret without knowledge of the dynamics of the free pool, as it can also be affected by edema and inflammation.[14] A quantitative approach to MT that separately factors in the contributions of the free pool and the bound pool, using an exchange signal model, is therefore highly desirable in the assessment of patients with acute, subacute or chronic cardiac remodeling and without the need for contrast injection.

In this study, we developed a cardiac model-based quantitative MT (qMT) mapping approach that seeks to study the contribution of the free pool and the bound pool in myocardial scar. This is achieved by using off-resonance preparation pulses and a two-pool exchange signal model to quantify the myocardial pool size ratio (PSR) and bound pool T2 (T_2^B). The PSR accounts for most of the signal but it relates to both the free and the bound pools; however, in combination with T_2^B (only bound pool), it may be possible to separately characterize the role of the bound and free pools in the cardiac remodeling process.

2 | METHODS

A sequence for contrast-free quantitative 2D myocardial scar imaging is proposed, consisting of five MT-weighted (MTw) spoiled gradient echo (SPGR) images, with variable MT preparations (FA and off-resonance frequency), as shown in Figure 1 and Table 1. To enable data acquisition in a single breath-hold with an acquisition window of <140 ms to minimize cardiac motion the five MT contrasts are acquired in one dummy shot and two imaging shots (ie, in 15 heartbeats). Novel model-based MT mapping (qMT) is performed using a two-pool exchange signal model and dictionary matching to quantify the PSR and bound pool T2. The signal model was developed and first validated using 25 MTw images on a bovine serum albumin (BSA) phantom and in vivo human thigh muscle, which was considered the reference standard. A protocol with only five MTw images was later designed to allow for breath-held cardiac imaging, using an optimization algorithm to determine the sequence parameters (MT FA and off-resonance frequency) that maximized the determination coefficient of the match (see Equation 4). The proposed myocardial qMT was tested in 10 healthy subjects and 5 patients with myocardial fibrosis. The study was approved by our local research ethics committee, and written informed consent was obtained from all subjects. An overview of the proposed framework is shown in Figure 2, including image acquisition, reconstruction and post processing, dictionary generation and matching, and image analysis. Each of these steps is described hereafter.

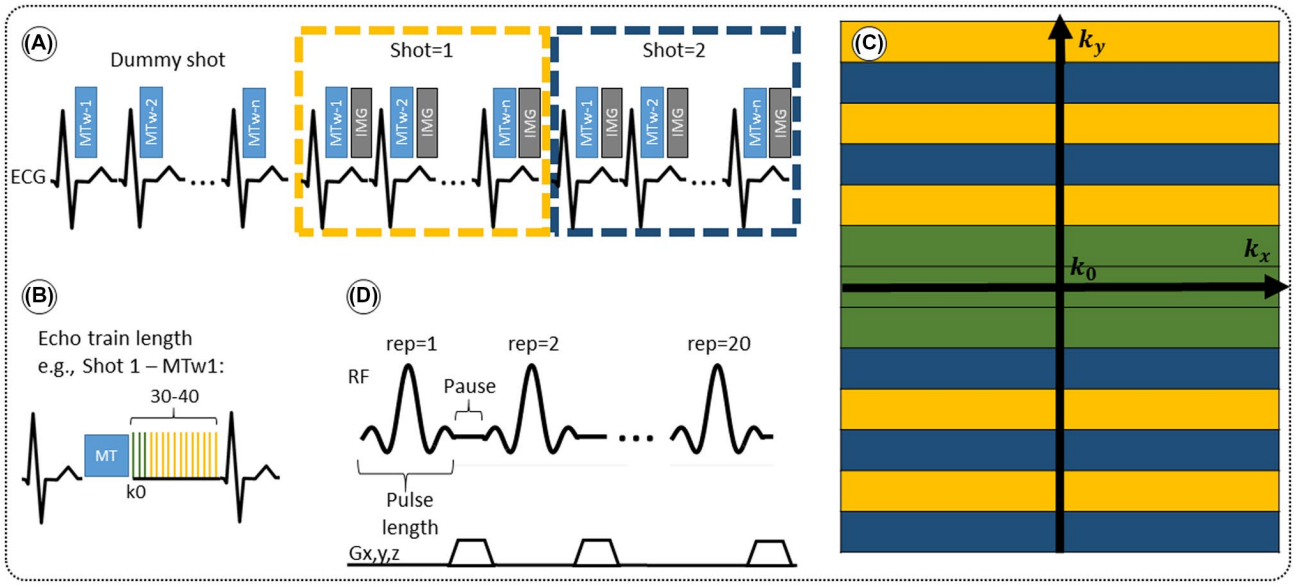

FIGURE 1 A, A scheme of the acquisition of "*n*" (eg, $n = 5$) interleaved MT-weighted 2D slices in two shots (ie, each MT-weighted k-space data set is acquired in two heartbeats), including a "dummy" shot made up of "*n*" heartbeats. A train of MT preparation pulse and an imaging module are played out in every heartbeat. B, A scheme of the imaging module applied for each image on each shot, consisting of 30-40 profiles (echo train length). C, A scheme of the acquisition of k-space in two shots (yellow/blue) with a centric profile, the center of k-space being sampled on every shot. (D) A scheme of the MT preparation module, consisting of a train of 20 identical sinc-shaped pulses at a given ΔF offset frequency and FA, with spoiler gradients played out during a brief pause period between each pulse

TABLE 1 Main sequence parameters for the MT preparation and imaging modules

MT Prep pulses			SPGR Readout	
MTw1	ΔF offset	1.5 kHz	Echo Train Length	36
	MT flipangle/peak B1	540 °/ 1.72 uT	# Shots	2
MTw2	ΔF offset	4.0 kHz	Bandwidth	500 Hz
	MT flipangle/peak B1	360°/1.14 uT	TE/TR	1.9/3.8 ms
MTw3	ΔF offset	0.9 kHz	Resolution	2.0 × 2.0 mm 2
	MT flipangle/peak B1	630°/2.01 uT	Slice Thick.	8 mm
MTw4	ΔF offset	2.9 kHz	FA	15 °
	MT flipangle/peak B1	450°/1.43 uT	Accel.	GRAPPA
MTw5	ΔF offset	2.1 kHz	Accel. Factor	2
	MT flipangle/peak B1	800°/2.54 uT		
All	Bandwidth	268 Hz		
	Length	20.48 ms		
	Repetitions	20		

SPGR: spoiled gradient echo, ΔF: freq. offset.

2.1 | Signal model

Let us consider a system where most spins have generally free motion (pool: A) and are at thermal equilibrium with a net magnetization M_0^A, while a small fraction of them is bound to macromolecules (pool: B) and have net magnetization M_0^B. It has been shown that for such system, the magnetization exchange between both pools can be represented by the so-called binary spin-bath model,[15] a specific case of the Bloch-McConnell equations[16] where the size of pool $A \gg B$. A steady-state solution to this set of coupled differential equations requires typically long RF preparation (>few seconds); however, a transient approach using extended phase graphs (EPGs) simulation has been recently proposed.[17]

The EPG framework analyses the system's magnetization response in terms of its *configuration states*,[18] which can be described as Fourier transforms (FTs) of the spatial magnetization components. In this space, the net magnetization dephasing caused by spatially variant gradients over

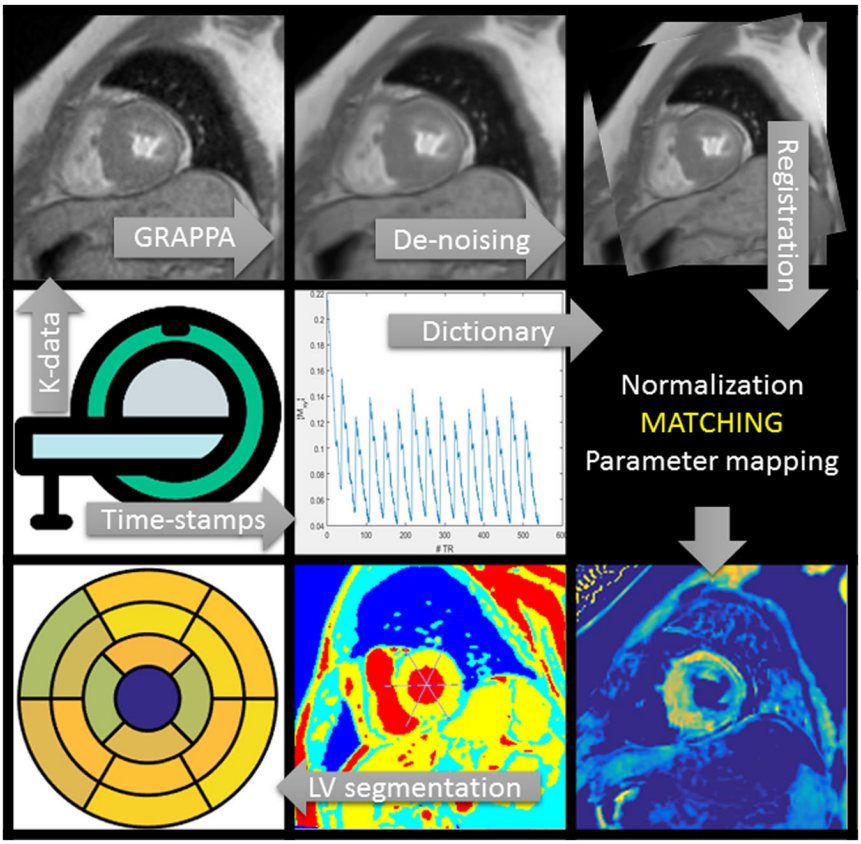

FIGURE 2 A diagram or data flow chart of the present study is shown. Acquired MR data are reconstructed with GRAPPA, followed by low-rank-based denoising and registration to align the different MT-weighted images. A dictionary is generated informed by literature free pool relaxation rates, the MR sequence (read-out) time stamps and other fundamental sequence parameters (TR, TE, FA, number of segments, etc.). After MR data and dictionary entries are self-normalized, a least-squares matching is performed (on a pixel-wise basis) to obtain the qMT parameter maps. Manual segmentation of the left-ventricle (LV) is performed on subjects for comparison and analysis

an entire ensemble of spins within a volume V is uniquely described by **k**, making computation much more efficient. The interactions with RF pulses, gradients, and the effects of relaxation and exchange are all represented by simple matrix operators. The EPG-X method extends the classic framework, to include a fourth configuration state,[17] that is, $\left[\tilde{F}_+, \tilde{F}_-, \tilde{Z}_A, \tilde{Z}_B\right]^T$, where $\tilde{Z}_B$ is as a FT of the bound pool's longitudinal magnetization, M_Z^B. The evolution of $\tilde{Z}_B$ is coupled to $\tilde{Z}_A$ via first order forward and backward exchange rates: k_f (or kf) and k_B. Because the time scale of the decay of transverse magnetization in the bound pool is very short (<20 μs), it is assumed to decay instantaneously. For this reason, only the exchange between longitudinal magnetizations is considered into the model. Another consequence of this instantaneous decay is that for the bound pool, RF excitation can be totally described as an instant saturation of the longitudinal magnetization at a certain rate W, proportional to RF power deposition, ω_1^2, and the bound pool's line absorption profile, g_B,

$$W(2\pi\Delta) = \pi\omega_1{}^2 g_B\left(2\pi\Delta, T_2^B\right) \tag{1}$$

where Δ is the offset frequency of the irradiation. In the case of a shaped RF pulse, Equation (1) can be generalized,[19] integrating over time for the duration of the pulse so that a time average of the saturation rate is obtained: $-\overline{W}$. The absorption profile g_B depends on Δ with a super-Lorentzian form, typical of partially ordered materials and semi-solids where the dipolar Hamiltonian does not average to zero over time. The width of the super-Lorentzian form is characterized by the T2 of the bound pool, T_2^B, and can be obtained as[20]:

$$g_B\left(2\pi\Delta, T_2^B\right) = \sqrt{2/\pi}\, T_2^B \int_0^{\pi/2} \frac{e^{-2\frac{\left(2\pi\Delta T_2^B\right)^2}{\left(3cos^2\theta-1\right)^2}}}{\left|3cos^2\theta-1\right|} \sin\theta d\theta \tag{2}$$

To further simplify the calculation of $\overline{W}$, the time-variant amplitude of the RF pulse in Equation (1) can be approximated by a time-constant value using Ramani's continuous wave power-equivalent formula.[21]

In our electrocardiograph (ECG)-triggered cardiac implementation, each MT preparation pulse is simulated by the RF transition operator $\boldsymbol{T}$ acting onto the longitudinal states $Z_n = [\tilde{Z}_A, \tilde{Z}_B]$ as,

$$\boldsymbol{T} = \begin{bmatrix} 1 & 0 \\ 0 & e^{-\overline{W}\tau_{RF}} \end{bmatrix} \tag{3}$$

That is, the effect on the bound pool is modelled by the average of the RF saturation rate $-\overline{W}$ times the length of the RF pulse τ_{RF}, while the longitudinal magnetization of the free water pool is not disturbed. This assumption is based on the use of low bandwidth sinc shaped MT pulses, high

off-resonance frequencies (>900 Hz) and simulation data reported in Supporting Information (Figure S1, which is available online).

After the transition operator, the evolution along the entire length of the pulse (plus any waiting/pause time between pulses) is governed by exchange and relaxation[17]:

$$\dot{F}_n = \begin{bmatrix} -\frac{1}{T_2^A} & 0 \\ 0 & -\frac{1}{T_2^A} \end{bmatrix} F_n \tag{4}$$

$$\dot{Z}_n = \begin{bmatrix} -\frac{1}{T_1^A} - k_f & k_B \\ k_f & -\frac{1}{T_2^B} - k_B \end{bmatrix} Z_n$$

Where $F_n = [\tilde{F}_+, \tilde{F}_-]$ represents the free pool's transverse configuration states. A SPGR acquisition immediately follows the train of MT preparation RF pulses, as also described in Ref. 17. Exchange and relaxation operators are applied again during waiting time between heartbeats.

2.2 | MRI sequence

A number of n MT-weighted images are acquired with an interleaved acquisition in $3 \times n$ consecutive heartbeats (as shown in Figure 1A, for $n = 5$) on a 1.5T scanner (Magnetom Aera, Siemens Healthcare, Erlangen, Germany). During the first n dummy heartbeats, MT preparation pulses are played out without any imaging readout, to achieve a (pseudo) *steady state* at the beginning the following $2 \times n$ heartbeats, when the *dual shot* image acquisition is performed. Each shot is made up of two modules performed in one heartbeat: (1) an MT preparation train of off-resonance RF pulses, and (2) an SPGR imaging module that collects only half of the entire k-space data. The interleaved acquisition aims at reducing (respiratory motion induced) mis-alignment between the MT weighted images. The MT preparation module consists of a train of 20 identical *sinc*-shaped RF pulses with a given frequency offset and FA. The imaging module consists of an SPGR sequence with Cartesian k-space sampling, centric reordering, and twofold accelerated GRAPPA acquisition.[22]

In a BSA phantom and in vivo human thigh muscle the sequence was applied with $n = 25$ different MT-weighted images. An acquisition protocol with $n = 5$ was used for cardiac in vivo imaging, due to the time restriction imposed by the subjects' ability to hold their breath. Different combinations of off-resonance frequencies and FAs were investigated for the 5 MT pre-pulses and the combination that resembled best the results obtained with 25 MT pre-pulses was used for all subsequent experiments.

2.3 | Image reconstruction and post-processing

The MTw images were reconstructed inline using the scanner software (Syngo E11C, Siemens Healthcare, Erlangen, Germany). In order to reduce noise, correct for motion misalignment between images due to variable heart rate and imperfect breath-holding, and generate a normalized input for the dictionary matching, we performed three off-line (MATLAB v. R2017b) post-processing steps:

1. Denoising: all MTw images were jointly denoised using a multi-contrast patch-based low-rank denoising technique,[23] which has been recently proposed to accelerate quantitative mapping without significant loss in accuracy.
2. Registration: all MTw images are motion aligned using an affine image registration procedure.[24]
3. Normalization: each (magnitude) MTw image is divided by the pixel-wise overall mean signal value along the contrast (MTw) dimension.

2.4 | Dictionary matching

A dictionary of possible signal evolutions is created using the model described before. Subject-specific ECG time stamps are incorporated in the signal simulation to make the model less sensitive to heart-rate variations.

Each entry in the dictionary is a vector of as many elements as MTw images. After computation, magnitude entries are normalized by the mean of all its elements. The maximum size of a single dictionary (with three free parameters: k_f, T_2^B, and PSR) was approximately 42k entries.

The vector difference between measured data and every dictionary entry is computed, for every pixel, to compute the parametric maps. The entry with highest determination coefficient R^2 is matched,

$$R^2 = 1 - \frac{\sum_{i=1}^{n} (m_i - f_i)^2}{\sum_{i=1}^{n} (m_i - \bar{m})^2} \tag{5}$$

where m_i is measured data point for the i-th MT weighting (for a given pixel), f_i is the corresponding i-th fitted value, $\bar{m}$ is the mean of all MT weighted data points (for a given pixel), and n is number of MTw acquisitions.

2.5 | Optimization and validation in phantoms

First, a BSA phantom consisting of four samples of different albumin concentrations (5%, 8%, 10% & 15%) was made following the description by Koenig et al.[25] The goal of this

BSA study was to optimize a sequence with five MT weightings for in vivo myocardial applications.

In summary, a reference protocol was implemented comprising 25 images with 25 distinct MT weightings (at fivedifferent frequency offsets log-spaced between 1 and 7.7 kHz and five different MT FAs linearly spaced between 360 and 800°) partly based on previous work by the authors.[26] Next, MT parameter maps were calculated based on dictionary matching using all the acquired MT images and (independently acquired) T1 and T2 maps. Then, PSR and T_2^B values were calculated for all possible combinations of five MT weightings and the best combination was chosen based on maximizing the accuracy of the parameter values and the coefficient of determination of the match. A detailed protocol is presented in Supporting Information (Text S2).

2.6 | In vivo validation in human thigh muscle

In the second part of this study, a validation of the model in vivo in human thigh muscle was performed in order to test the sequence in a molecular environment closer to that of the myocardium, that is, collagen and other proteins present in human muscle, to obtain qMT parameters that could be used to guide our target cardiac study. The 25-MTw protocol (as described above) was acquired in a healthy subject and compared to the prospective acquisition of the proposed 5-MTw protocol. The parameter k_f ($k_f = 4.2$ Hz) was estimated from the 25-MTw protocol selecting a muscle region of interest (ROI) and using a dictionary with three degrees of freedom: PSR (range = 0-15, step = 0.1, [%]), T_2^B (range = 5-20, step = 0.5, [us]) and k_f (range = 1-5, step = 0.5, [Hz]). PSR and T_2^B parameter maps were then created using a dictionary with two degrees of freedom (k_f fixed to the obtained value): PSR (range = 0-15, step = 0.1, [%]), T_2^B (range = 2-20, step = 2, [us]). The parameters maps from the 5-MTw protocol were obtained with the same parameter ranges, fixed inputs, and degrees of freedom.

2.7 | In vivo cardiac imaging study: healthy subjects and patients

Ten healthy subjects (age: 30 ± 3 y, 7 female) and five patients with myocardial fibrosis (age: 62 ± 10, all male) underwent MRI with the 5-MTw protocol (prior to contrast administration in patients). MT preparation pulse parameters and imaging parameters are described in Table 1 and were derived from the optimization described before.

Patients undergoing a clinically indicated cardiac MR (CMR) at our institution were selected based on the likelihood of having ischemic or non-ischemic myocardial scar (including previous imaging findings, clinical history and age). The only exclusion criterion was the presence of a pacemaker (due to the associated likelihood of imaging artefacts). All patients followed the standard cardiac MR (CMR) protocol at our institution, including cine, T1 mapping, early gadolinium enhancement (EGE) and LGE imaging, in addition to the proposed sequence. T2 mapping was additionally performed in two patients (P1 and P4). The characterization of the patients' heart disease/etiology in this study were obtained from the CMR report, based on the entirety of the imaging findings and additional information made available by the referring clinician.

The proposed sequence was acquired in short axis, in patients prior to contrast agent injection, with the following relevant parameters: ECG-triggered acquisition with mid-diastolic data acquisition of <140 ms, number of slices = 10-14, spatial resolution = 2 × 2 mm (interpolated to 1.4 × 1.4 mm), slice thickness = 8 mm, and scanning time approximately 15 s per slice. In patients, phase sensitive inversion recovery (PSIR) LGE acquisition was performed 12-15 min after injection of *Gadovist* contrast agent for comparison purposes. LGE imaging parameters included a balanced steady-state free precession (bSSFP) sequence with TE/TR = 1.2/3.0, FA = 45°, short-axis stack, variable field of view, in plane spatial resolution = 1.4 × 1.4 mm^2, slice thickness 8 mm and number of slices = 10-14.

Parameter maps were created using a dictionary with one degree of freedom: PSR (range = 0-15, step = 0.02, [%]). Free pool relaxation rates were fixed to mean reported values for healthy myocardium: $T_2^A = 53$ ms,[27,28] and $T_1^A = 950$ ms.[29] Exchange rate k_f was fixed to the value found for human thigh muscle (Table 2). A fixed value of T_2^B was used in parameter mapping (from human thigh muscle, Table 2) and a dictionary of T_2^B (range = 2-20, step = 2, [us]) was used in ROI-based calculations.

The 5-MTw protocol was repeated three separate times over four mid-ventricular slices in one non-scar patient to assess reproducibility of measurements.

2.8 | Statistics

Manual segmentation of the myocardium was performed over one basal, one mid and one apical slices in healthy subjects, using one of the denoised MTw images (MTw #3, Δ = 0.9 kHz, FA = 630°) to create a mask, following the American Heart Association (AHA) 16-segment model.[30] The mask was then applied onto the parameter maps and measurements of mean and SD were taken for each AHA segment and for every subject.

Delineation of scar and remote ROIs in patients (in PSR and LGE slices) was performed by two independent readers

TABLE 2 MT parameter measurements in BSA phantom and human thigh muscle (muscle ROI)

	BSA 15%		BSA 10%		BSA 8%		BSA 5%		Thigh Muscle		Unit
	25 pt	5 pt	25 pt	5 pt	25 pt	5 pt	25 pt	5 pt	25 pt	5 pt	
Fixed parameters											
T1A	848	848	1052	1052	1251	1251	1503	1503	1022	1022	ms
T2A	77	77	112	112	157	157	238	238	52	52	ms
KF	3.0	3.0	3.0	3.0	3.0	3.0	3.0	3.0	4.2	4.2	Hz
Free parameters											
PSR	9.4 ± 0.2*	8.0 ± 1.5*	5.9 ± 0.1	5.9 ± 0.7	4.5 ± 0.1	4.4 ± 0.7	2.9 ± 0.1	3.0 ± 0.4	10.9 ± 0.3	10.8 ± 0.8	%
T2B	6.7 ± 0.7	6.8 ± 0.5	6.5 ± 0.9	6.8 ± 0.5	6.6 ± 0.5	6.8 ± 0.4	6.7 ± 0.4	6.8 ± 0.5	6.4 ± 0.4	6.5 ± 0.7	μs

PSR, pool size ratio; T2B, T2 of the bound pool; KF, forward exchange rate; T1A, T1 of the free pool; T2A, T2 of the free pool; BSA, sovine serum albumin.

*$P < .05$.

(one blinded to LGE) with experience in CMR. A third experienced reader provided qualitative assessment and advice. PSR mean and SD values per ROI were measured for each patient and averaged between readers. Total ROI areas were also recorded and percentage area differences (Δarea) between corresponding LGE and PSR slices are reported. Co-registration of PSR and LGE slices was done manually/visually since the number of slices and the field of view did not always coincide. MT/PSR and LGE images were acquired with a delay of up to 20 min (due to contrast injection), often causing patient mis-alignment, movement of arms, or the need to increase the LGE's field of view beyond the limits of the MT acquisition.

PSR measurements in pectoral muscle ROIs within the field of view (FOV) of every apical slice were obtained both in healthy subjects and patients.

3 | RESULTS

3.1 | Phantom and in vivo model validation

Using the 25-MTw protocol, mean values of PSR for the BSA 15% and BSA 10% phantom vials were comparable with previous reports,[31,32] at PSR = 9.4 ± 0.2% and PSR = 5.9 ± 0.7, respectively (Table 2). There was good agreement between PSR and T_2^B mean values measured with the 25-MTw and the 5-MTw protocols, except for a small reduction in the PSR value for the BSA 15% vial with the 5-MTw acquisition (BSA15%: 25 pt =9.4 ± 0.2% vs. 5 pt = 8.0 ± 1.5%). T_2^B values were similar for all vials and both protocols. Table 2 shows parameter measurements for all phantom vials and protocols. For the 25-MTw protocol, k_f was almost constant across all samples, with a mean value $k_f = 3.0 \pm 1.2$ Hz.

PSR and T_2^B thigh muscle parameter maps generated with protocol 25-MTw and 5-MTw are shown in Figure 3A. Mean values of PSR (PSR = 10.9 ± 0.3%), T_2^B (T_2^B = 6.4 ± 0.4 us) and k_f (k_f = 4.2 ± 1.2 Hz) estimated from the 25-MTw protocol were found within the range of previously reported *in vivo* thigh muscle studies.[33] No statistical significance between mean PSR and T_2^B values was found when comparing the 25-MTw and the 5–MTw protocols, as shown in Table 2.

PSR estimation was robust against the choice of MT FA (FA = 0-800°) and ΔF (0-7.7 kHz) with mean PSR = 10.9 ± 0.1 [%] at 95% confidence interval (CI), median 11.1 [%] and range 10.0 to 11.4 [%], as shown in Figure 3B. The estimation of T_2^B was found slightly more dependent on variation of MT FA and ΔF, with mean $T_2^B = 6.5 \pm 0.2$ [us] at 95% CI, median 6.0 [us] and range 4.0 to 8.0 [us].

The number of free and fixed parameters for the model-based dictionary was determined based on simulations. The

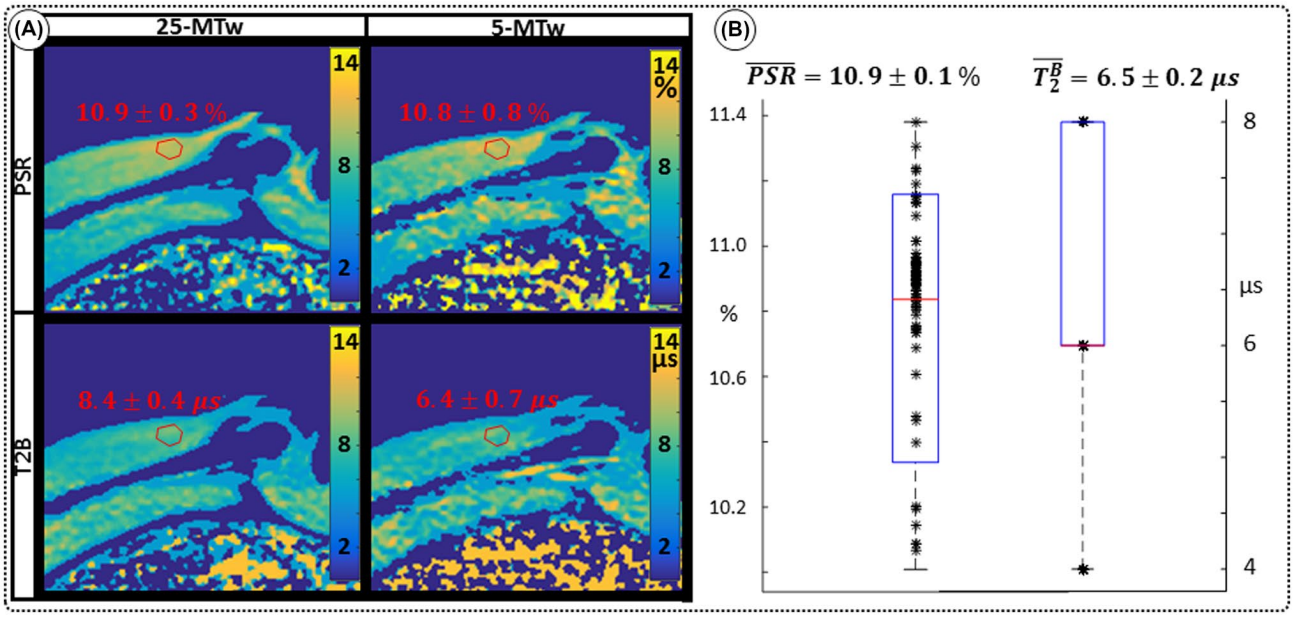

FIGURE 3 A, Comparison of PSR and T_2^B maps obtained in thigh muscle of a healthy subject using two qMT protocols with either 25 images or 5 images (sagittal view). Good agreement is observed between the 25-MTw and 5-MTw measurements for both phantom and in vivo scans. B, Assessment of robustness of estimation of PSR (left) and T_2^B (right) against variation of FA (FA = 0-800°) and off-resonance frequency (ΔF = 0-7.7 kHz) for 80 random 5MTw combinations in a thigh muscle ROI. Box plots show median (red), interquartile range (blue) and full range (black) statistics

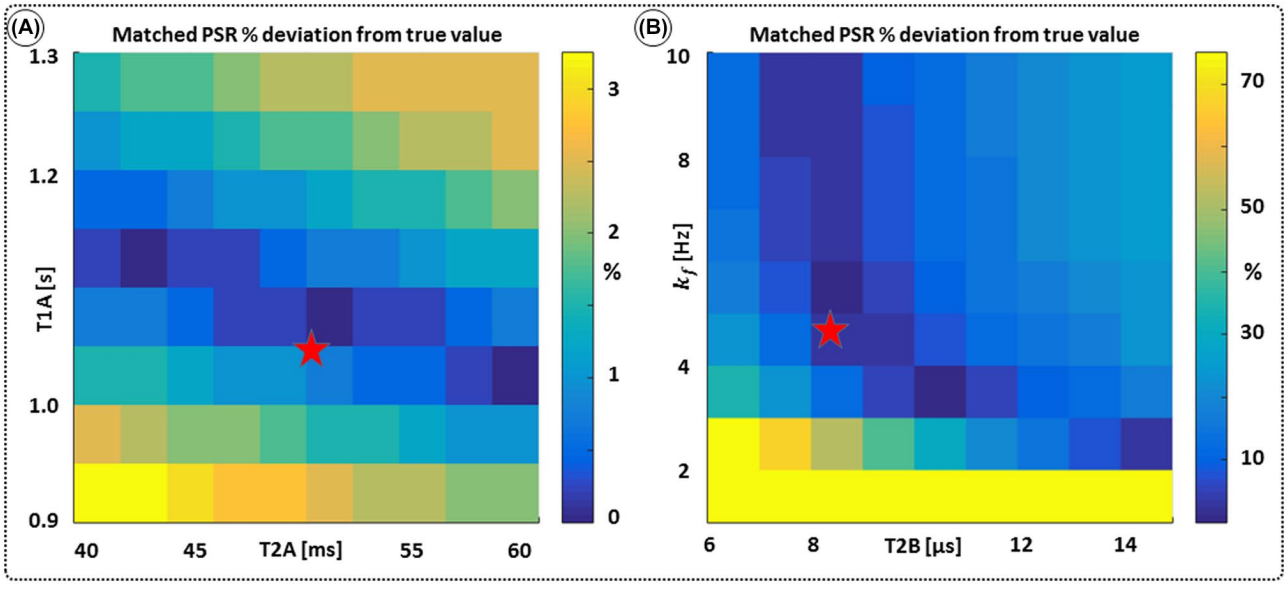

FIGURE 4 A (fixed) simulated signal vector (PSR = 4%, T_2^B = 8.4 us, k_f = 4 Hz, T_1^A = 1050 ms, T_2^A = 50 ms) is matched with a range of fixed T_1^A/T_2^A combinations ($T_1^A = 900-1300$ ms, $T_2^A = 40-60$ ms), showing extremely low sensitivity (<3%) to changes in both T_1^A and T_2^A. (B) The same signal vector is matched with a range of k_f/T_2^B combinations, showing moderate sensitivity to T_2^B, while k_f sensitivity is limited to $k_f < 4$ Hz (here, the true value)

sensitivity to free pool relaxation rates (T_1^A, T_2^A) of the proposed sequence is shown in a simulated matching experiment in Figure 4A, where a (fixed) typical myocardial signal vector (PSR = 4%, T_2^B = 8.4 us, k_f = 4 Hz, T_1^A = 1050 ms, T_2^A = 50 ms) was matched with a range of fixed T_1^A/T_2^A combinations ($T_1^A = 900-1300$ ms, $T_2^A = 40-60$ ms), resulting in a PSR match error under 4% for the entire range of combinations. The same myocardial signal vector was also matched with a range of fixed T_2^B/k_f combinations, as shown in Figure 4B. The error in PSR match was up to ≈12% for ±1 us error in

T_2^B. On the contrary, the error in PSR match was below 5% for any k_f values similar and above those found in muscle (eg, $k_f = 4.9$ Hz[32]).

3.2 | Cardiac study: healthy subjects

Mapping of myocardial T_2^B showed large and non-smooth spatial variation, at times outside the expected range for muscle, 5-15 us.[15,34] However, matching the average signal of a mid-septum myocardial ROI resulted in $T_2^B = 6.6 \pm 1.3us$ ($n = 10$), which is within the expected range and comparable to other muscle tissue, for example, thigh muscle (see above). For this reason, PSR parameter maps were calculated with a fixed T_2^B (and k_f) using the values that were validated in thigh muscle (see above).

Denoised images showed an average difference of 1.2% in the mean value of the signal in a mid-ventricular septal ROI compared with original (non-denoised) images. The regularization parameter (σ) was set at $\sigma = 4 \cdot 10^{-3}$ to obtain the best compromise between accuracy and precision (see Supporting Information Figure S3A). This resulted in an average difference in the estimation of PSR of 0.6 [PSR %] while the SD was reduced from 2.6 to 0.4 [PSR %] in the same ROI (see Supporting Information, Figure S3B-E). All images presented hereon were denoised following the procedure described earlier and all parameter measurements presented are derived from denoised images.

In healthy subjects, global left ventricular PSR was 4.30 ± 0.65%. Average intra-segment PSR SD was 0.65 [%] and inter-segment SD was 0.54 [%]. Average pectoral muscle PSR was 6.92 ± 0.21% (Table 3). PSR maps generally had spatially uniform appearance with a small tendency of reduced PSR toward anterior and antero-septal regions. One basal slice and one apical slice are shown for two representative healthy subjects in Figure 5. A myocardial segment bull's eye plot of PSR mean values and SD (respectively) averaged across all subjects is also shown in Figure 5E,F.

In the reproducibility experiment, the SD of mean PSR from mid-ventricular septum over all measurements ($n = 12$) was 0.33 [PSR %], a deviation of 5.4% from the mean value.

Eight out of 10 healthy subjects had stable heart rate under 62 bpm. Two healthy subjects had stable heart rate between 71 and 82 bpm. The PSR maps of the latter did not show a statistically significant difference from the global (all-subjects) average.

Whole body specific absorption rate (SAR) estimation was below 0.15 W/kg or 10% of the normal controlled standard in all volunteers.

3.3 | Cardiac study: patients

Four patients (P1-P4) showed myocardial enhancement on LGE images, with findings indicative of previous myocardial infarction. One patient, P5, showed a focal area of epicardial

TABLE 3 PSR measurements in pectoral muscle and myocardium (core scar and remote) ROIs in patients and remote myocardium in healthy subjects

	Slice#	Gender	Age	Remote PSR [%]	Core scar PSR [%]	LGE/PSR Δarea [%]	Pectoral muscle PSR [%]	Scar transmurality
Healthy subjects, $n = 10$								
Mean			30 ± 3	4.30 ± 0.65			6.92 ± 0.21	
Patients Group A								
P1	1	M	65	4.84 ± 0.15	2.78 ± 0.16	11.61 ± 0.79	6.52 ± 0.66	Near transmural
	2			4.03 ± 0.92	1.78 ± 0.07	6.74 ± 1.16		
	3			3.44 ± 0.71	2.66 ± 0.09	10.41 ± 1.09		
P2	1	M	64	4.75 ± 0.30	3.19 ± 0.17	45.65 ± 4.57	6.88 ± 0.16	75% subendocardial
	2			4.93 ± 0.45	3.13 ± 0.12	19.20 ± 15.56		
P3	1	M	59	5.85 ± 0.59	3.93 ± 0.09	41.17 ± 5.75	7.08 ± 0.07	Transmural
Mean group A			**63 ± 3**	**4.64 ± 0.82***	**2.91 ± 0.71***	**22.47 ± 16.78**	**6.83 ± 0.28**	
Patients Group B								
P4	1	M	48	4.91 ± 0.22	3.11 ± 0.69	12.70 ± 6.83	5.18 ± 0.09	50-75% subendocardial
P5	1	M	75	4.72 ± 0.81	4.35 ± 0.56	39.82 ± 1.97	7.45 ± 0.31	Focal area
Mean all patients			**62 ± 10**	**4.68 ± 0.70***	**3.12 ± 0.78***	**23.41 ± 16.0**	**6.62 ± 0.87**	

LGE vs. PSR scar area difference (Δarea) also shown in patients.

*$P < .002$.

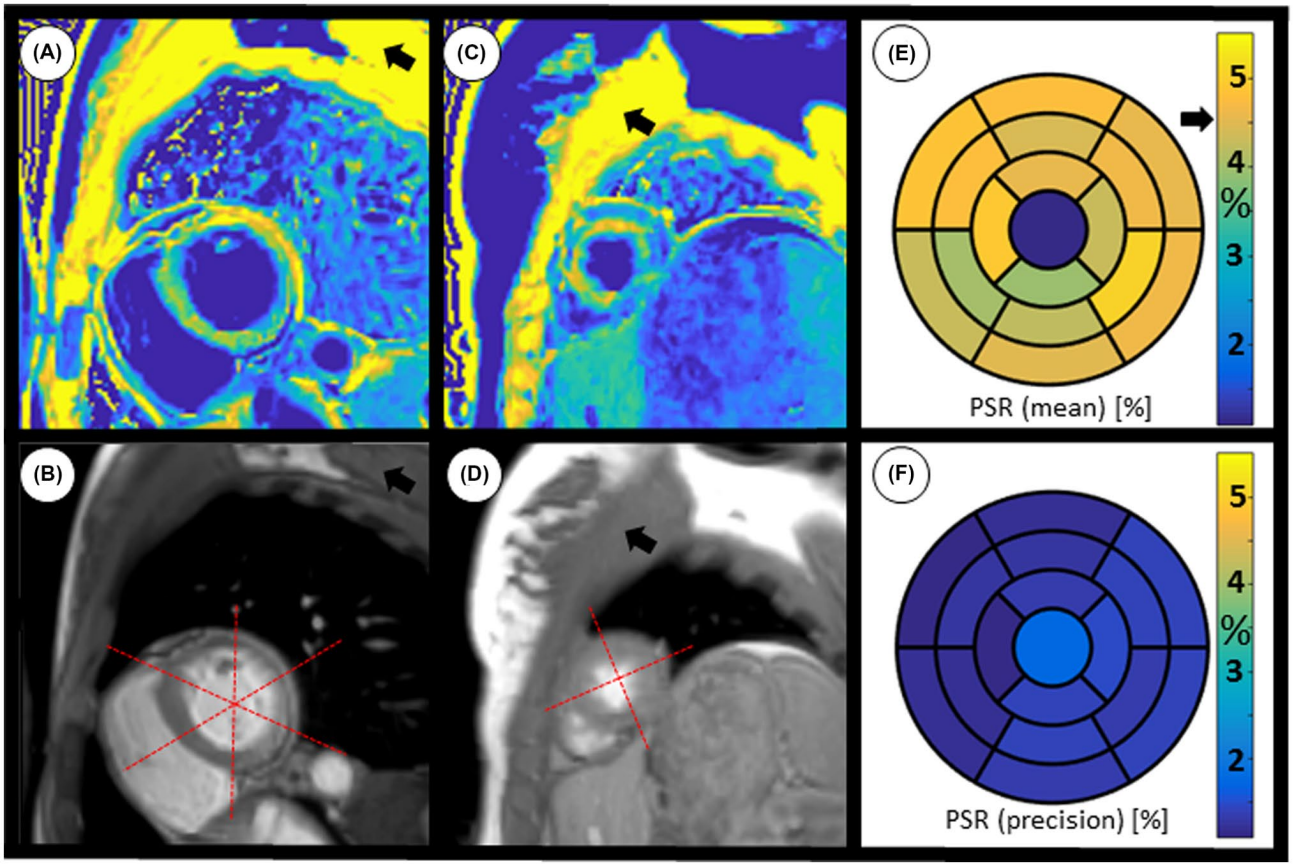

FIGURE 5 A,B, PSR map and one of the corresponding MTw images ($\Delta = 0.9$ kHz, FA = 630°) of a myocardial (short-axis) basal slice of healthy subject (H1, female, 28 years). C,D, PSR map and one of the corresponding MTw images ($\Delta = 0.9$ kHz, FA = 630°) of a myocardial (short-axis) apical slice of healthy subject (H2, female, 37 y). Some areas of skeletal muscle used for measurements are shown (black arrows). E,F, Mean and SD of PSR across the myocardium, respectively, averaged across all healthy subjects ($n = 10$), measured using manual segmentation based on the American Heart Association model.[29] Overall mean left ventricle PSR was 4.30 ± 0.65 %, see black arrow in (E)

to mid-wall myocardial enhancement consistent with a non-ischemic scar distribution, possibly due to prior myocarditis.

P1 showed evidence of lipomatous metaplasia in the lateral wall and previous transmural myocardial infarction of the inferolateral wall (left circumflex coronary artery territory) of unknown age (Figure 6, P1); however, T2 maps demonstrated non-elevated myocardial T2 values within the region of scar (infarct ROI: T2 = 48.6 ± 4.3, remote T2 = 49.2 ± 2.7), suggesting that the infarct is not acute/subacute.

P2 showed evidence of transmural myocardial infarction in the right coronary artery (RCA) territory on LGE (Figure 6, P2) and stress-induced perfusion abnormalities with preserved viability in the left anterior descending (LAD) territory (not shown in Figure). Also, the early phase (ie, EGE) showed evidence of microvascular obstruction (MVO) in the inferior wall. P2 had had coronary artery bypass grafting (CABG) with saphenous vein graft to RCA approximately 8 years earlier. T2 weighted images were not available.

P3 showed evidence of previous transmural myocardial infarction in the LAD (Figure 6, P3, far left) and localized MVO at basal anterior septum in the early phase (Figure 6, P3, far right). T2 weighted images were not available.

P4 had a subacute presentation with a near transmural infarct in the territory of the first diagonal (D1) coronary artery with corresponding signal increase in T2 maps (infarct ROI: T2 = 59.6 ± 3.4, remote T2 = 46.2 ± 2.3), on a background of a prior chronic infarct in the LAD territory.

P5 showed evidence of a non-ischemic distribution of LGE (mid-wall, septal) in a patient with sarcoidosis. T2 weighted images were not available.

ROIs likely to correspond with scar in PSR maps were identified by both readers in three patients (P1-P3) and ROIs drawn by the blinded reader are shown in Figure 6. One reader also identified ROIs likely to correspond with scar in patients P4 and P5, shown in Figure 7. Small areas of slightly reduced or increased PSR were also observed, which did not correlate with LGE.

PSR measurements and LGE/PSR area differences for each patient are reported in Table 3. All patients showed reduced PSR in myocardial regions likely to be scar tissue that corresponded with location and extent of LGE

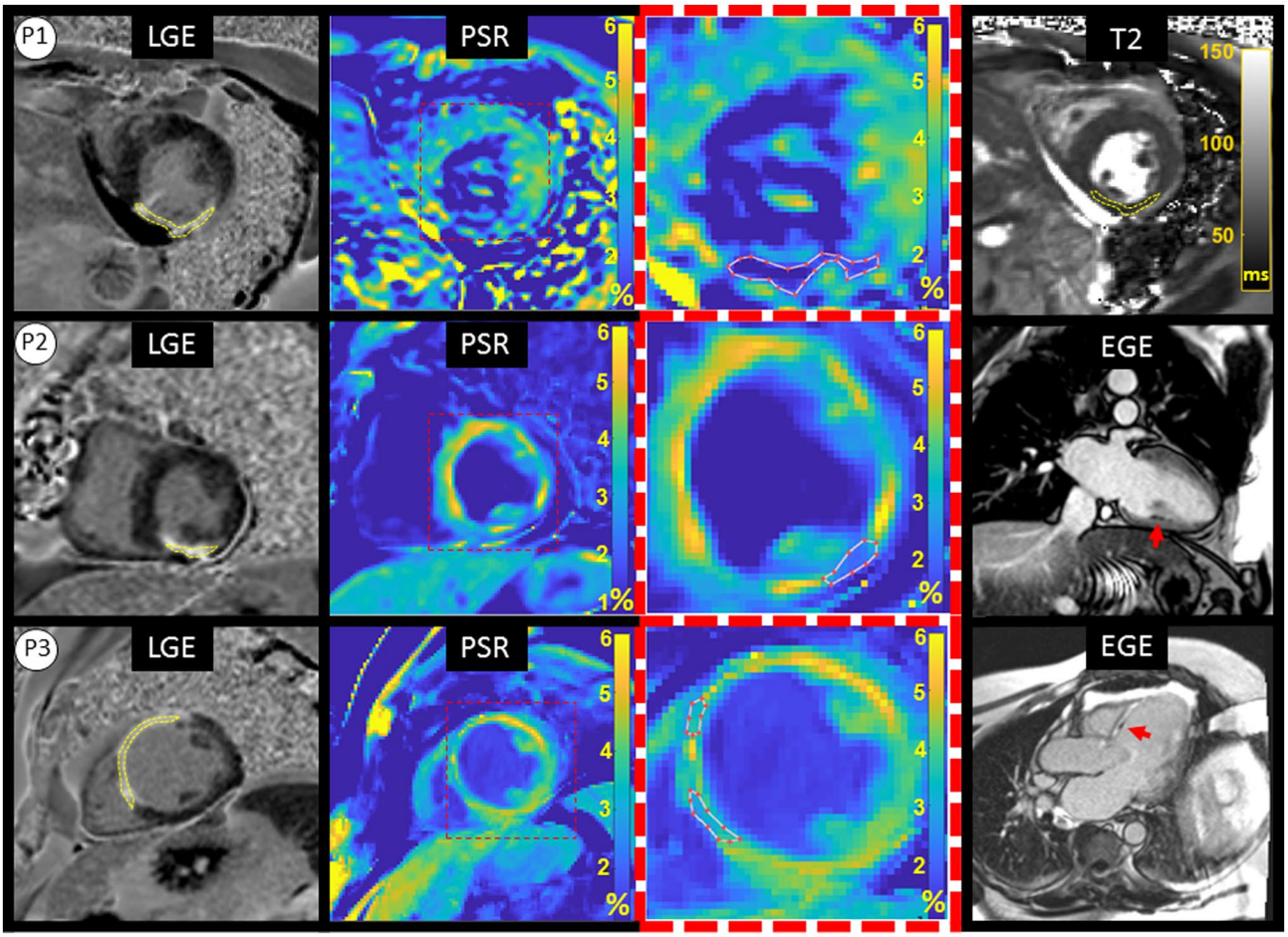

FIGURE 6 The left and left-middle columns show LGE and PSR co-registered short-axis slices for each patient, the middle right column represents a zoomed PSR frame centered in the left ventricle and the far right column represents additional imaging related to inflammation or MVO. Upper row, Patient P1 mid-ventricle slice with near transmural LGE enhancement (yellow dashed line) of the inferior and lateral walls and normal T2 (far right). Middle Row, Patient P2 basal slice with subendocardial LGE enhancement (yellow dashed line) in the basal infero-septal, inferior and infero-lateral segments. MVO observed in (two-chamber view) EGE, far right. Bottom row, Patient P3 mid-ventricular slice with transmural LGE enhancement in mid-distal anterior and anterior septal segments, local micro-vascular obstruction observed in EGE (three-chamber view, far right). All patients present clear reduction in PSR values in correlation with LGE

enhancement. Average remote myocardium PSR in patients P1-P3 was 4.64 ± 0.82% and average core scar PSR was 2.91 ± 0.35% ($P < .002$), giving an average difference of 1.7% PSR. Similar results were found when including all patients P1-P5 (4.68 ± 0.70% vs. 3.12 ± 0.78%, for remote and core scar, respectively). Average LGE/PSR scar area difference in patients P1-P3 was 22.47 ± 16.78% (range 6.74 to 45.65%), while values for P4-P5 fell within a similar range (12.7%-39.8%).

Average pectoral muscle PSR in all patients was similar to the same measurement in healthy subjects (6.62 ± 0.87% vs. 6.92 ± 0.21%, p = NS).

4 | DISCUSSION

Parameter maps of PSR and T_2^B for BSA phantom and human thigh muscle yielded accurate estimations, in agreement with previous studies. The proposed 5-MTw myocardial approach showed good agreement with the 25-MTw protocol for the estimation of PSR, thus, making it feasible to acquire a quantitative 2D myocardial PSR map in vivo, in a single breath-hold.

PSR values obtained from multiple measurements within a single subject were reproducible and heart rate differences among healthy subjects did not appear to affect the PSR maps. To the best of our knowledge, this is the first time model-based quantitative MT mapping has been performed in the human heart. Furthermore, the PSR variations among healthy subjects (ie, 0.65% PSR) were less than half the average difference between core scar and remote measurements in patients (ie, 1.7% PSR), which showed that the precision for measuring remote myocardium in vivo with the proposed sequence may be sufficient for identifying at least some types of fibrosis.

In our cardiac study, ROIs were identified by two readers in patients with strong likelihood of having ischemic scar

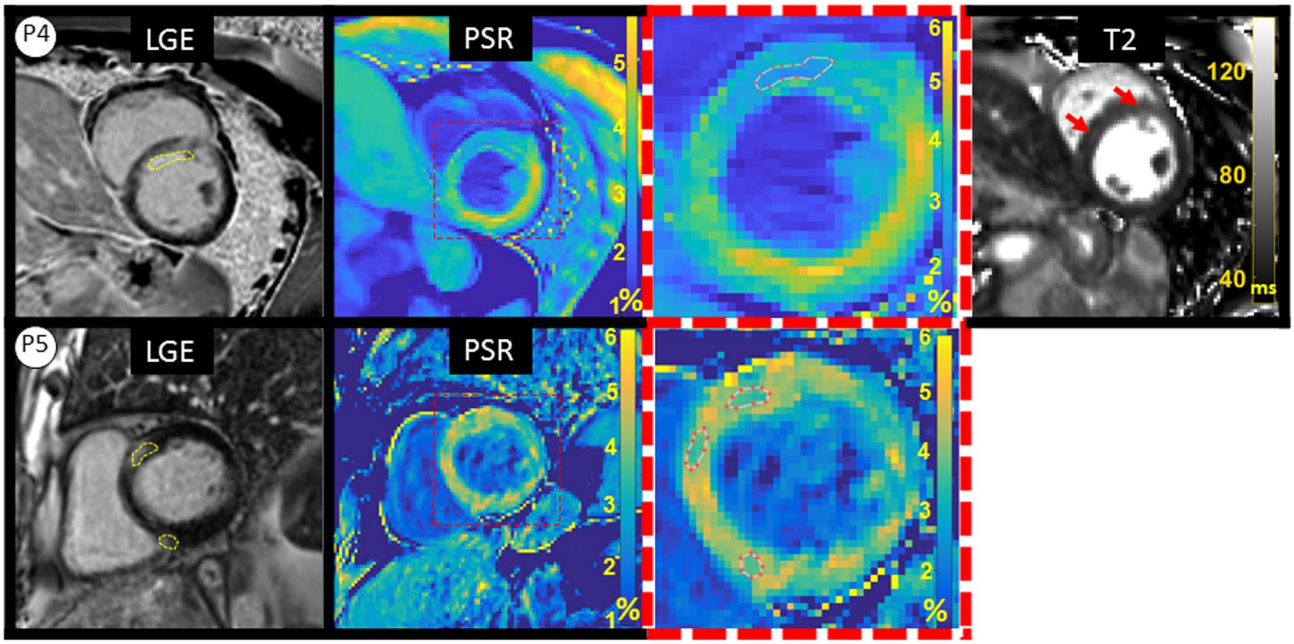

FIGURE 7 Far left and left-middle columns show LGE and PSR co-registered short-axis slices for each patient, the right middle column represents a zoomed PSR frame centered in the left ventricle and the far right column represents additional imaging related to inflammation. Upper row, Patient P4 with subendocardial LGE enhancement (yellow dashed line) in mid antero-septal, anterior, and infero-septal segments. T2 values were increased in ROI associated with LGE enhancement (T2 map, short-axis slice, far right). Bottom row, Patient P5 basal slice with mid-myocardial focal LGE enhancement in anterior and inferior segments (yellow dashed line). Both patients present moderate reduction in PSR values in correlation with LGE

(P1-P3). On the contrary, in patients with a likelihood of recent infarction or non-ischemic scar (P4-P5), ROIs were identified by only one of the readers (not blinded to LGE). Despite moderate dispersion or heterogeneity of the signal in the myocardium in all subjects, the findings showed evidence of reduced MT saturation effects in infarct areas in all patients. It is possible that some of the PSR differences (within the infarcted myocardium) in P1 versus P2-P4 can be explained by chronicity, since the evidence of MVO (in P2 and P3) or increased T2 (in P4) is suggestive of at least subacute presentation. However, additional studies may be needed to determine all the physical/physiological factors driving the imaging contrast.

Our results did not show evidence of an increase of the bound pool in the presence of replacement fibrosis/collagen, that is, in the chronic MI patients. On the contrary, a reduction of the MT effects was observed, which is consistent with findings in chronic myocardial infarction in rats by Scholz et al,[35] findings of fibrosis in end-stage renal disease (ESRD) patients by Stromp et al,[36] and reports from Duan et al[13] in 15-mo (average) post MI patients using a hybrid T1/MT –weighted sequence. The proposed sequence may present advantages over Duan et al and Stromp et al in terms of quantification of the bound pool and potential specificity to fibrosis, since the cited approaches rely on combining the MT contrast with T1 and/or T2 weighting.

The observed reduction of the MT effects may be due to cardiac remodeling factors, other than collagen deposition, having a more substantial effect in the MT signal, such as necrosis and the associated loss of mitochondrial protein content,[37] or an increase in water mobility within collagenous scar.[38] Other tissue characterization techniques based on the excitation of the bound pool, such as T1ρ, have found similar results in chronic MI, with reported increased relaxation times in 8-wk old scar in swine[38] and diffuse myocardial fibrosis in patients.[39]

One of the main challenges of a cardiac MRI study is to find the right compromise between spatial resolution, signal-to-noise ratio (SNR) and motion. In this study, we decided to minimize the cardiac motion by keeping the acquisition window relatively short (<140 ms), thereby resulting in a dual shot sequence (each MT weighted image is acquired in two heartbeats) with five MT weightings with an acceptable breath-hold duration of 15 consecutive heartbeats, which was tolerated by most patients. However, other sources of patient motion during the acquisition and/or errors in the co-registration of the MT weighted images may have been associated with areas of slightly increased or reduced PSR, which did not correlate with LGE findings in patients. Also, a low SNR may have hindered pixel-wise estimation of T_2^B in the myocardium, given that the weight of T_2^B effects on the signal is far more subtle than the weight of PSR. This is supported by the fact that ROI-based estimation, with intrinsically higher SNR, gave results within the expected range. This led us to choose a fixed value for T_2^B to estimate PSR in the myocardium. It is to note, however, that giving a fixed

(non-myocardium) value to T_2^B may have introduced a bias in the PSR measurements, as shown in our simulations. Further studies are needed to enable reproducible mapping of T_2^B in the myocardium. Specifically, since the estimation of T_2^B in our thigh muscle model was also found to depend moderately on variations of MT FA and ΔF.

It is possible that T_2^B maps of the heart may be obtained by reducing the weight of noise and motion artefacts in the fitting. This may be approached in two different ways: increasing the number of images (weightings) and/or significantly increasing the SNR. The SPGR readout that was used in this study is relatively robust against B0 and B1 inhomogeneity at 1.5 T and was, therefore, our choice to avoid bias in parameter fitting; however, the TR is long and was not practical to pursue a single shot acquisition that would have allowed more MT weightings within a single breath-hold, as it would have led to an acquisition window of ≈280 ms. Lower spatial resolution or high acceleration factors may enable single shot qMT mapping and are subject to future investigations. Alternatively, a 3D approach with short acquisition window and the proposed 5 MT weightings may be feasible in a short scan time,[23] providing a significant increase in SNR that may enable the estimation of PSR and T_2^B; however, respiratory motion during a free-breathing acquisition would need to be carefully addressed.

Other limitations of this study may be the use of fixed T_1^A and T_2^A rates measured with techniques that do not model the effects of two pools (eg, MOLLI or T2-prep bSSFP). However, simulations showed that the maximum error introduced into the calculation of PSR due to this effect is likely to be less than 3%. Similarly, simulations showed that B1 variations affect matched PSR values at a proportional rate of close to 2:1 (see Supporting Information Figure S4). Moreover, Chow et al has reported[40] B1 deviations of up to 20-30% across the chest (including the lungs) but only smooth variations of approximately 5-10% across left ventricle ROIs at 1.5 T. Thus, B1 inhomogeneity could potentially generate inaccurate or biased PSR values, however, it is unlikely to explain or correlate with the observed regional variations of PSR (associated with scar) in post MI patients.

Regarding the patient study, the relatively large age difference between healthy subjects and patients constitutes another limitation, as well as the small size of the patient cohort. In terms of accuracy necessary to identify clinical fibrosis, a larger number of clinically well-defined patients with infarcts of defined chronicity may be needed to establish a "true" PSR value for infarcted myocardium. Furthermore, other factors that may affect the MT effects should be also taken into account when assessing diseased myocardium, such as large increases in pH, which have been shown to affect the MT exchange rate.[41]

5 | CONCLUSIONS

We have demonstrated that human myocardial qMT mapping is feasible and can be done with a 15 heartbeat qMT imaging protocol in a single breath-hold. Furthermore, PSR variations among healthy subjects (ie, 0.65% PSR) were less than 50% the average PSR difference between core scar and remote myocardium in patients (ie, 1.7% PSR). Thus, the results showed that the precision for measuring PSR in remote myocardium in vivo with the proposed sequence may be sufficient for identifying focal fibrosis.

ACKNOWLEDGMENTS

This work was supported by (1) the EPSRC Centre for Doctoral Training in Medical Imaging (EP/L015226/1), (2) EPSRC grants EP/P001009/1 and EP/P007619, (3) the Wellcome EPSRC Centre for Medical Engineering (NS/A000049/1 and WT 203148/Z/16/Z), and (4) the Department of Health via the National Institute for Health Research (NIHR) Cardiovascular Health Technology Cooperative (HTC) and comprehensive Biomedical Research Centre awarded to Guy's & St Thomas' NHS Foundation Trust in partnership with King's College London and King's College Hospital NHS Foundation Trust. KL is co-funded by Siemens Healthcare GmbH.

CONFLICT OF INTEREST

Radhouene Neji is an employee of Siemens Healthcare Limited (UK).

ORCID

Karina López https://orcid.org/0000-0003-1477-8879
Aurelien Bustin https://orcid.org/0000-0002-2845-8617
Shaihan J. Malik https://orcid.org/0000-0001-8925-9032
Rui Pedro A. G. Teixeira https://orcid.org/0000-0001-6508-9315
Sébastien Roujol https://orcid.org/0000-0002-7146-0552

REFERENCES

1. Flett AS, Hasleton J, Cook C, et al. Evaluation of techniques for the quantification of myocardial scar of differing etiology using cardiac magnetic resonance. *JACC Cardiovasc Imaging*. 2011;4:150-156.
2. Mewton N, Liu CY, Croisille P, Bluemke D, Lima JA. Assessment of myocardial fibrosis with cardiovascular magnetic resonance. *J Am Coll Cardiol*. 2011;57:891-903.
3. Kellman P, Wilson JR, Xue H, Ugander M, Arai AE. Extracellular volume fraction mapping in the myocardium, part 1: Evaluation of an automated method. *J Cardiovasc Magn Reson*. 2012;14:63.
4. Bull S, White SK, Piechnik SK, et al. Human non-contrast T1 values and correlation with histology in diffuse fibrosis. *Heart*. 2013;99:932-937.

5. van Oorschot JW, Gho JM, van Hout GP, et al. Endogenous contrast MRI of cardiac fibrosis: Beyond late gadolinium enhancement. *J Magn Reson Imaging*. 2015;41:1181-1189.
6. Kuo PH, Kanal E, Abu-Alfa AK, Cowper SE. Gadolinium-based MR contrast agents and nephrogenic systemic fibrosis. *Radiology*. 2007;242:647-649.
7. Robert P, Fingerhut S, Factor C, et al. One-year retention of gadolinium in the brain: Comparison of gadodiamide and gadoterate meglumine in a rodent model. *Radiology*. 2018;288:424-433.
8. Phinikaridou A, Andia ME, Saha P, Modarai B, Smith A, Botnar RM. In vivo magnetization transfer and diffusion-weighted magnetic resonance imaging detects thrombus composition in a mouse model of deep vein thrombosis. *Circ Cardiovasc Imaging*. 2013;6:433-440.
9. Crooijmans HJ, Ruder TD, Zech WD, et al. Cardiovascular magnetization transfer ratio imaging compared with histology: A postmortem study. *J Magn Reson Imaging*. 2014;40:915-919.
10. Wolff SD, Balaban RS. Magnetization transfer contrast (MTC) and tissue water proton relaxation in vivo. *Magn Reson Med*. 1989;10:135-144.
11. Stromp TA, Leung SW, Andres KN, et al. Gadolinium free cardiovascular magnetic resonance with 2-point Cine balanced steady state free precession. *J Cardiovasc Magn Reson*. 2015;17:90.
12. Weber OM, Speier P, Scheffler K, Bieri O. Assessment of magnetization transfer effects in myocardial tissue using balanced steady-state free precession (bSSFP) cine MRI. *Magn Reson Med*. 2009;62:699-705.
13. Duan C, Zhu Y, Jang J, et al. Non-contrast myocardial infarct scar assessment using a hybrid native T1 and magnetization transfer imaging sequence at 1.5T. *Magn Reson Med*. 2019;81:3192-3201.
14. Vavasour IM, Laule C, Li DK, Traboulsee AL, MacKay AL. Is the magnetization transfer ratio a marker for myelin in multiple sclerosis? *J Magn Reson Imaging*. 2011;33:713-718.
15. Sled JG, Pike GB. Quantitative imaging of magnetization transfer exchange and relaxation properties in vivo using MRI. *Magn Reson Med*. 2001;46:923-931.
16. Henkelman RM, Huang X, Xiang QS, Stanisz GJ, Swanson SD, Bronskill MJ. Quantitative interpretation of magnetization transfer. *Magn Reson Med*. 1993;29:759-766.
17. Malik SJ, Teixeira R, Hajnal JV. Extended phase graph formalism for systems with magnetization transfer and exchange. *Magn Reson Med*. 2018;80:767-779.
18. Weigel M. Extended phase graphs: dephasing, RF pulses, and echoes - Pure and simple. *J Magn Reson Imaging*. 2015;41:266-295.
19. Graham SJ, Henkelman RM. Understanding pulsed magnetization transfer. *J Magn Reson Imaging*. 1997;7:903-912.
20. Morrison C, Stanisz G, Henkelman RM. Modeling magnetization transfer for biological-like systems using a semi-solid pool with a super-Lorentzian lineshape and dipolar reservoir. *J Magn Reson B*. 1995;108:103-113.
21. Ramani A, Dalton C, Miller DH, Tofts PS, Barker GJ. Precise estimate of fundamental in-vivo MT parameters in human brain in clinically feasible times. *Magn Reson Imaging*. 2002;20:721-731.
22. Griswold MA, Jakob PM, Heidemann RM, et al. Generalized autocalibrating partially parallel acquisitions (GRAPPA). *Magn Reson Med*. 2002;47:1202-1210.
23. Bustin A, Lima da Cruz G, Jaubert O, Lopez K, Botnar RM, Prieto C. High-dimensionality undersampled patch-based reconstruction (HD-PROST) for accelerated multi-contrast MRI. *Magn Reson Med*. 2019;81:3705-3719.
24. Modat M, Ridgway GR, Taylor ZA, et al. Fast free-form deformation using graphics processing units. *Comput Methods Programs Biomed*. 2010;98:278-284.
25. Koenig SH, Brown RD 3rd, Ugolini R. Magnetization transfer in cross-linked bovine serum albumin solutions at 200 MHz: A model for tissue. *Magn Reson Med*. 1993;29:311-316.
26. Lopez K, Neji R, Mukherjee RK, et al. Contrast-free high-resolution 3D magnetization transfer imaging for simultaneous myocardial scar and cardiac vein visualization. *MAGMA*. 2020;33:627–640.
27. Giri S, Chung YC, Merchant A, et al. T2 quantification for improved detection of myocardial edema. *J Cardiovasc Magn Reson*. 2009;11:56.
28. Huang TY, Liu YJ, Stemmer A, Poncelet BP. T2 measurement of the human myocardium using a T2-prepared transient-state TrueFISP sequence. *Magn Reson Med*. 2007;57:960-966.
29. Dabir D, Child N, Kalra A, et al. Reference values for healthy human myocardium using a T1 mapping methodology: Results from the International T1 Multicenter cardiovascular magnetic resonance study. *J Cardiovasc Magn Reson*. 2014;16:69.
30. Cerqueira MD, Weissman NJ, Dilsizian V, et al. American heart association writing group on myocardial S, registration for cardiac I. Standardized myocardial segmentation and nomenclature for tomographic imaging of the heart. A statement for healthcare professionals from the cardiac imaging committee of the council on clinical cardiology of the American heart association. *Circulation*. 2002;105:539-542.
31. Dortch RD, Li K, Gochberg DF, et al. Quantitative magnetization transfer imaging in human brain at 3 T via selective inversion recovery. *Magn Reson Med*. 2011;66:1346-1352.
32. Gochberg DF, Gore JC. Quantitative magnetization transfer imaging via selective inversion recovery with short repetition times. *Magn Reson Med*. 2007;57:437-441.
33. Li K, Dortch RD, Kroop SF, et al. A rapid approach for quantitative magnetization transfer imaging in thigh muscles using the pulsed saturation method. *Magn Reson Imaging*. 2015;33:709-717.
34. Sinclair CD, Samson RS, Thomas DL, et al. Quantitative magnetization transfer in in vivo healthy human skeletal muscle at 3 T. *Magn Reson Med*. 2010;64:1739-1748.
35. Scholz TD, Hoyt RF, DeLeonardis JR, Ceckler TL, Balaban RS. Water-macromolecular proton magnetization transfer in infarcted myocardium: A method to enhance magnetic resonance image contrast. *Magn Reson Med*. 1995;33:178-184.
36. Stromp TA, Spear TJ, Holtkamp RM, et al. Quantitative gadolinium-free cardiac fibrosis imaging in end stage renal disease patients reveals a longitudinal correlation with structural and functional decline. *Sci Rep*. 2018;8:16972.
37. Ward K, Schussheim AE, Balaban RS. Contribution of mitochondria to cardiac muscle water/macromolecule proton magnetization transfer. *Magn Reson Med*. 2003;50:1312-1316.
38. Witschey WR, Zsido GA, Koomalsingh K, et al. In vivo chronic myocardial infarction characterization by spin locked cardiovascular magnetic resonance. *J Cardiovasc Magn Reson*. 2012;14:37.
39. van Oorschot JW, Guclu F, de Jong S, et al. Endogenous assessment of diffuse myocardial fibrosis in patients with T1rho -mapping. *J Magn Reson Imaging*. 2017;45:132-138.

40. Chow K, Paterson I, Thompson R. Radiofrequency (B1) field mapping in the heart and lungs using a HASTE double angle method. *Proc Intl Soc Mag Reson Med*. 2008;16:1244.
41. Kennan RP, Richardson KA, Zhong J, Maryanski MJ, Gore JC. The effects of cross-link density and chemical exchange on magnetization transfer in polyacrylamide gels. *J Magn Reson B*. 1996;110:267-277.

SUPPORTING INFORMATION

Additional Supporting Information may be found online in the Supporting Information section.

FIGURE S1 Comparison of comparison of EPGX-MT vs MAMT models for using flip angles 360°, 540° and 720° as a function of frequency offset Δf. Small discrepancies between the methods increase at lower frequencies and higher flip angles

TEXT S2 Algorithm for optimization and validation in phantoms

FIGURE S3 Optimization of image de-noising and impact on PSR estimation. (A) Left axis shows the difference between the mean values of original and denoised images ("Δ mean" line) for a myocardial ROI with varying regularization level σ, while the right axis shows the ratio between the mean value and standard deviation of the same ROI for each regularized image. (B-C) Example mid-ventricular slice showing an original (non-denoised) MT weighted image and the obtained PSR parameter map, respectively. (D-E) Denoised MT weighted image and its respective PSR parameter map, at optimal regularization level σ = 4e-4

FIGURE S4 Simulated PSR matches (blue line) showing "PSR deviation" from the true value as a function of "B1 deviation" or inhomogeneity for a 5-MTw protocol. The relationship between B1 and PSR deviation appears proportional approximately 2:1, as reflected by the best fit line (red) with equation "y = 0.42*x + 0.55"

How to cite this article: López K, Neji R, Bustin A, et al. Quantitative magnetization transfer imaging for non-contrast enhanced detection of myocardial fibrosis. *Magn Reson Med*. 2020;00:1–15. https://doi.org/10.1002/mrm.28577